Nanoporous Structures

Deutsche Ausgabe: DOI: 10.1002/ange.201603666
Internationale Ausgabe: DOI: 10.1002/anie.201603666

A Titanium-Doped SiO_x Passivation Layer for Greatly Enhanced Performance of a Hematite-Based Photoelectrochemical System

*Hyo-Jin Ahn, Ki-Yong Yoon, Myung-Jun Kwak, and Ji-Hyun Jang**

Abstract: *This study introduces an in situ fabrication of nanoporous hematite with a Ti-doped SiO_x passivation layer for a high-performance water-splitting system. The nanoporous hematite with a Ti-doped SiO_x layer (Ti-(SiO_x/np-Fe_2O_3)) has a photocurrent density of 2.44 mA cm^{-2} at 1.23 V_{RHE} and 3.70 mA cm^{-2} at 1.50 V_{RHE}. When a cobalt phosphate co-catalyst was applied to Ti-(SiO_x/np-Fe_2O_3), the photocurrent density reached 3.19 mA cm^{-2} at 1.23 V_{RHE} with stability, which shows great potential of the use of the Ti-doped SiO_x layer with a synergistic effect of decreased charge recombination, the increased number of active sites, and the reduced hole-diffusion pathway from the hematite to the electrolyte.*

Owing to the environmental pollution from the fossil energy, the demand for clean energy has gradually increased.[1] Photoelectrochemical (PEC) water splitting is a promising clean energy generating system that captures and stores solar energy by splitting water into hydrogen and oxygen gases.[2] Many semiconductors, including TiO_2, ZnO, CdSe, CdS, Ta_3N_5, and Fe_2O_3, are used as photoanode materials that can generate photoexcited electron/hole pairs[3] in PEC systems. Among them, α-Fe_2O_3 (hematite), which has a small band gap of 2.1 eV, natural abundance, high theoretical solar-to-hydrogen (STH) efficiency (16.8 %), and an appropriate energy band position against water-oxidation potential (1.23 V_{RHE}), has been suggested as a superior photoanode for the PEC system.[3d,4] However, because of its short hole-diffusion length, high electron–hole recombination rate, poor charge mobility, weak oxygen evolution reaction (OER) properties, and slow charge-transfer kinetics, achieving significant STH efficiency and performance of α-Fe_2O_3 is still limited.[5] To address the limitations of α-Fe_2O_3, a high-surface-area hematite, such as nanoporous α-Fe_2O_3 and 3D inverse opal α-Fe_2O_3, which successfully enhanced the PEC performance by increasing the number of the water oxidation sites and reducing the hole diffusion pathway, have been investigated.[6] Alternatively, several passivation layers, including the SnO,[7] IrO_2,[8] Ga_2O_3,[8] and Al_2O_3[9] thin layers, have been applied on α-Fe_2O_3 to enhance PEC performance and stability by reducing the onset potential of water-splitting reactions and by preventing direct contact between hematite and the electrolyte. The passivation layer protects the surface states that cause charge recombination by facilitating the charge extraction at the semiconductor–electrolyte interface.[10] However, most of the passivation layers used before are alkaline unstable or adhere poorly to the semiconductors, which results in low long-term stability of the PEC device in harsh aqueous solutions.[8,9]

Herein, we report a highly stable Ti-doped porous Fe_2O_3 photoanode in the working conditions with a thin passivation layer of Ti-doped amorphous SiO_x, fabricated in situ by a simple hydrothermal/annealing process. The Ti-doped SiO_x layer induced the creation of the nanopores in Ti-(SiO_x/np-Fe_2O_3) under high-temperature annealing conditions and facilitated the charge transfer by passivating the surface states of hematite, which resulted in enhanced PEC performance. The photocurrent density of the Ti-(SiO_x/np-Fe_2O_3) was 2.43 mA cm^{-2} at 1.23 V_{RHE}, which is about 200 % improved PEC efficiency over the conventional worm-like Ti-Fe_2O_3, and it was maintained for 20 h in alkaline electrolytes without deterioration. We attributed the superior photocurrent density obtained from Ti-(SiO_x/np-Fe_2O_3) to the combination of the protected surface states and increased surface area owing to the occurrence of nanosize pores. Finally, the photocurrent density further increased to 3.19 mA cm^{-2} at 1.23 V_{RHE} after we applied cobalt phosphate (Co-Pi) OER catalysts to the Ti-(SiO_x/np-Fe_2O_3).

Figure 1 shows the pore generation mechanism of Ti-(SiO_x/np-Fe_2O_3) caused by the presence of the Ti-SiO_x layer on the surface of Ti-FeOOH during the high temperature annealing process. For the fabrication of conventional worm-like Ti-Fe_2O_3 in Figure 1 a, Ti-FeOOH nanorods were hydrothermally grown on FTO glass with $FeCl_3 \cdot 6H_2O$ and $TiCl_3$ in a convection oven at 100 °C. The Ti-FeOOH sample (a, I) was then heated at 850 °C in the furnace to convert Ti-FeOOH into Ti-Fe_2O_3. Under these high-temperature conditions, the 30–50 nm thin Ti-FeOOH nanorods (Supporting Information, Figure S1 a) were coalesced due to partial melting accompanied by dehydration, grain-boundary motion (GBM), and oriented attachment (OA) to form worm-like shaped nonporous hematite with a 100 nm–150 nm major axis and 50 nm minor axis (II, Figure 1 c).[11] On the other hand, Ti-FeOOH (b, I) was first immersed in the solution of aminopropyltrimethoxysilane (APTMS) and $TiCl_3$ and heated at 100 °C to create a thin Ti-SiO_x layer[12] on the surface of Ti-FeOOH as shown in Figure 1 b (Ti-(SiO_x/FeOOH (II′)). The Ti-(SiO_x/FeOOH) was then annealed up to 850 °C to turn FeOOH into α-Fe_2O_3, evolving gases such as HCl and H_2O during the dehydration process.[13] The circa 20 % weight loss of APTMS/

[*] Dr. H. J. Ahn, K. Y. Yoon, M. J. Kwak, Prof. J. H. Jang
Center for Multidimensional Carbon Materials, Institute for Basic Science IBS, Ulsan 44919, Republic of Korea
Dr. H. J. Ahn, K. Y. Yoon, M. J. Kwak, Prof. J. H. Jang
School of Energy & Chemical Engineering, Low Dimensional Carbon Materials Center, UNIST, Ulsan 44919, Republic of Korea
E-mail: clau@unist.ac.kr

Supporting information for this article can be found under: http://dx.doi.org/10.1002/anie.201603666.

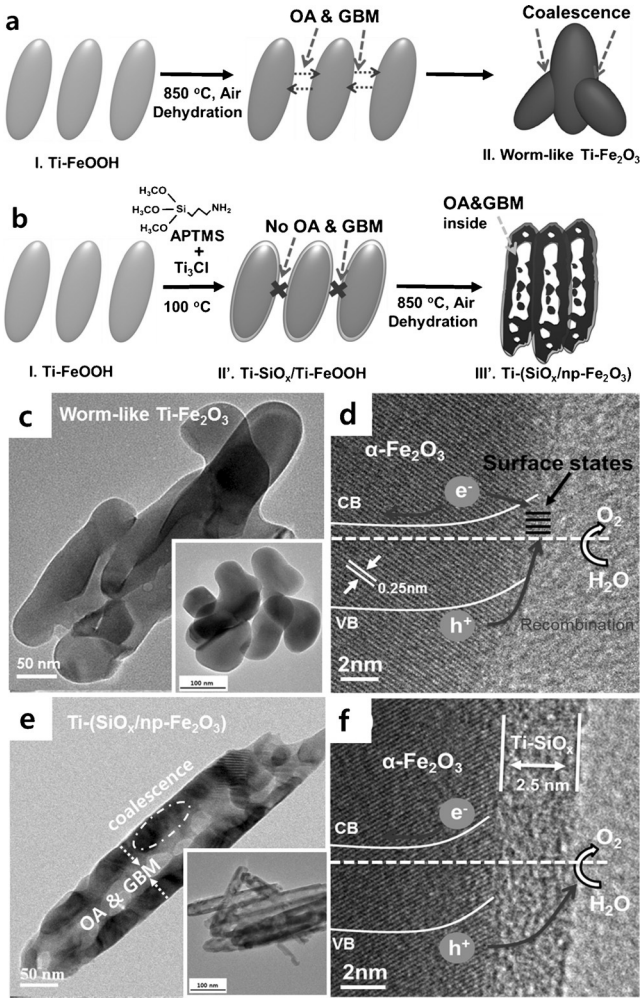

Figure 1. The fabrication procedures for a) conventional worm-like Ti-Fe_2O_3 and b) Ti-(SiO_x) layer-coated porous hematite (Ti-(SiO_x/Fe_2O_3)). a) I. Ti-doped FeOOH synthesized by hydrothermal growth; II. Coalescent Ti-Fe_2O_3 after heat treatment of Ti-FeOOH due to the oriented attachment (OA) and grain boundary motion (GBM) process. b) I. Ti-FeOOH before the APTMS treatment; II′. Ti-SiO_x coated Ti-FeOOH without the OA and GBM process between the rods; III′. Ti-(SiO_x/np-Fe_2O_3) with nanopores in the rods. c) TEM image of worm-like Ti-Fe_2O_3. d) High-magnification TEM image of a worm-like Ti-Fe_2O_3 in the boundary. e) TEM image of Ti-(SiO_x/np-Fe_2O_3). f) High magnification TEM image of Ti-(SiO_x/np-Fe_2O_3) in the boundary. The insets in (c) and (e) are low-magnification TEM images. The sketches in (d) and (f) show the simplified electron–hole transport mechanism.

$TiCl_3$ treated Ti-FeOOH in a temperature range from 100 °C to 400 °C in the TGA curve (Supporting Information, Figure S2) confirms the dehydration process in Ti-(SiO_x/np-Fe_2O_3).[14] Due to the presence of the rigid SiO_x layer, the freshly formed gases were entrapped inside Ti-(SiO_x/FeOOH), creating a vacancy during the annealing/solidifying process. The Ti-(SiO_x/FeOOH) nanorods did not merge (no GBM or OA) owing to the presence of the robust Ti-SiO_x layer, even at high-temperature annealing conditions. Instead, the GBM and OA process seems to occur inwards in each rod during the rearrangement/solidifying process caused by the newly generated vacancy in the annealing/cooling condition, creating Ti-(SiO_x/np-Fe_2O_3) with the many pores in the core and the thick frames in the shell, as shown in Figure 1b (III′) and Figure 1e. The Ti-(SiO_x/np-Fe_2O_3) in Figure 1e has cylinder-like structures consisting of 10–25 nm pores with a lattice spacing of 0.25 nm, matching a (110) plane of α-Fe_2O_3. Besides, it is clear that the 2.5–5 nm amorphous Ti-SiO_x layer covered α-Fe_2O_3, as shown in Figure 1d and the Supporting Information, Figure S3. Note that the crystallinity of the (110) plane of the original Fe_2O_3 was not deteriorated by the $TiCl_3$ or APTMS treatment as shown in the XRD data in the Supporting Information, Figure S4. The number of pores in the Ti-(SiO_x/np-Fe_2O_3) film increased with an increasing concentration of the Ti-APTMS solution and dipping time of Ti-FeOOH in the Ti-APTMS solution since full coverage coating of Ti-SiO_x with the thickness saturation of 2–5 nm hindered the evacuation of gases, as shown in the Supporting Information, Figures S5–S7. The surface area was increased by 2.5 times in the porous Ti-(SiO_x/np-Fe_2O_3) as shown in the BET data (Supporting Information, Figure S8). The illustrations in Figure 1d and f describe the electron–hole transport behavior in the band diagram of the devices when Ti-Fe_2O_3 or Ti-(SiO_x/np-Fe_2O_3) photoanodes were immersed in the electrolyte under irradiation conditions. The surface states in the band structure of α-Fe_2O_3 are known to cause a charge recombination resulting in poor water-oxidation properties (Figure 1d).[15] After applying 2.5–5 nm of the Ti-SiO_x passivation layer (Figure 1f; Supporting Information, Figure S3d), the OER properties of Ti-(SiO_x/np-Fe_2O_3) was enhanced by the protection of the surface states due to the presence of Ti-SiO_x interface between the electrolyte and α-Fe_2O_3.

To elucidate the composition of Ti-(SiO_x/np-Fe_2O_3), we conducted EDS and XPS analysis as shown in Figure 2 and the Supporting Information, Figures S9, S10. The TEM mapping data of Si, Ti, Fe, and O in Figures 2b,c confirmed the uniform dispersion of each element in Ti-(SiO_x/np-Fe_2O_3). The XPS spectra in Figures 2d,e show the Si 2p and Ti 2p peaks of the Ti-(SiO_x/np-Fe_2O_3). The binding energy at 98.76, 100.4, 101.23, and 102.9 eV in Figure 2d corresponds to Si^0,

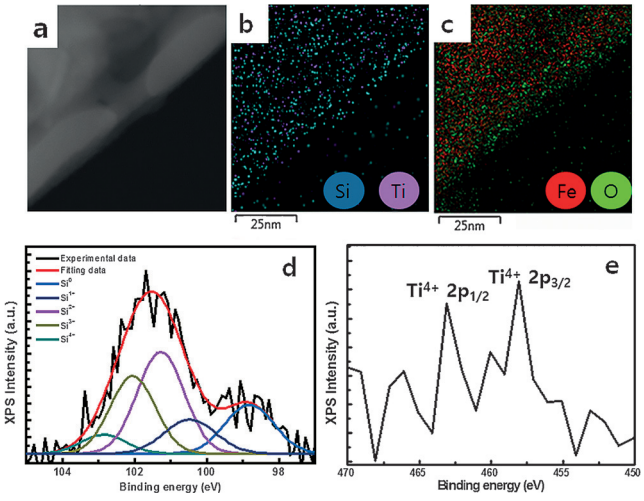

Figure 2. a)–c) TEM and EDS mapping images of Si, Ti, Fe, and O in the Ti-(SiO_x/np-Fe_2O_3), indicating uniform distribution of the ions. d), e) XPS spectra of the Si 2p (d) and Ti 2p (e) regions.

Si^{1+}, Si^{2+}, Si^{3+}, and Si^{4+}, respectively, suggesting that the silica thin film was partially oxidized ($X < 2$ in SiO_x, an amorphous phase).[16] It has been reported that the amorphous SiO_x layer can combine with the OH^- that was generated by splitting water in an alkaline solution to form a SiO_x:OH^- layer with a negatively charged surface.[17] As shown in the Supporting Information, Table S2 and Figure S11, the surface of Ti-(SiO_x/np-Fe_2O_3) is highly negatively charged at pH 13.0[17b] owing to the existence of the SiO_x:OH^- layer, which helps the fast and direct extraction of photogenerated holes from hematite to generate O_2 gas.[18] We also confirmed the increase in the XPS peak intensity at 531.1 eV, corresponding to adsorbed OH^- ions on Ti-(SiO_x/np-Fe_2O_3) after a 20 h stability test (Supporting Information, Figure S12a). Nevertheless, the XPS spectra of Si ions and morphology of Ti-SiO_x did not noticeably change after the 20 h stability test, suggesting that Si suboxides (Si^{1+}, Si^{2+}, and Si^{3+}) are able to provide stable water oxidation sites and the overall reaction is steady (Supporting Information, Figure S12), which confirms the good chemical stability. The XPS spectra of Ti 2p were found as two peaks: Ti^{3+} $2p_{1/2}$ at 461.06 eV and Ti^{4+} $2p_{3/2}$ at 458.08 eV.[19] The metal-ion-doped dielectric material was used as a conductive filament in the resistance random access memory device by reducing the resistivity of metal oxides through a hopping conduction mechanism and tunneling effect.[20] Therefore, the Ti ion-doped thin SiO_x film has a higher conductivity than the non-doped SiO_x layer and facilitates the charge transfer through the Ti-SiO_x layer (Supporting Information, Figure S13). We also observed that doping the SiO_x layer with other metal ions such as Ag and Au showed effects similar to the case of Ti doping (Supporting Information, Figure S14).

Figure 3a shows the *J*–*V* curve of the reference Ti-Fe_2O_3, Ti-(SiO_x/Fe_2O_3), and Ti-(SiO_x/np-Fe_2O_3) under AM 1.5 (100 mW cm^{-2}) illumination and dark conditions in a 1 M NaOH electrolyte solution with a three-cell electrode system. To compare the presence of the pores in Ti-Fe_2O_3, nonporous Ti-(SiO_x/Fe_2O_3) was prepared by simply dipping as-prepared worm-like Ti-Fe_2O_3 in a APTMS/$TiCl_3$ solution. After applying the Ti-SiO_x passivation layer, the dark onset potential (dotted lines) of the Ti-(SiO_x/Fe_2O_3) and Ti-(SiO_x/np-Fe_2O_3) was lower than that of Ti-Fe_2O_3, which indicates that Ti-SiO_x has good electrocatalytic properties for water oxidation, as explained in Figure 2. The photocurrent density and the onset potential of Ti-(SiO_x/np-Fe_2O_3) showed a significant increase to 2.44 mA cm^{-2} and a cathodic shift to 0.95 V_{RHE} from 1.23 mA cm^{-2} and 1.01V_{RHE} of Ti-Fe_2O_3 due to good OER properties by the reduction of the surface states (red vs. black), when both the Ti-SiO_x passivation layer and porous structures were applied as shown in Figure 3a. By solely applying a Ti-SiO_x passivation layer to a nonporous structure (Ti-(SiO_x/Fe_2O_3)), the onset potential shifted from 1.01 V_{RHE} to 0.92 V_{RHE}, but the photocurrent density increase stopped at 1.75 mA cm^{-2} at 1.23 V vs. RHE (blue vs. black). We attributed the further increase in the photocurrent density in Ti-(SiO_x/np-Fe_2O_3) over Ti-(SiO_x/Fe_2O_3) to the presence of nanopores that provided an increased number of reaction sites and decreased the path distance for photogenerated electron–hole transfer. The slightly lower absorption of Ti-(SiO_x/np-Fe_2O_3) due to the lower content of Fe_2O_3 surrounded by air holes inside the nanoporous photoanode[21] confirms that the Ti-SiO_x layer does not hinder the absorption of the photoanode in the UV/Vis range (Supporting Information, Figure S15). As confirmed by an increased surface area (Supporting Information, Figure S8), this was achieved by our synthetic procedure by which FeOOH was coated by the SiO_x layer first followed by the transformation to α-Fe_2O_3 accompanied by gas evaporation in the confined region. To analyze the electrochemical properties of the Ti-SiO_x and the charge transfer process at the surface of the electrolyte/Ti-SiO_x/Ti-Fe_2O_3, electrochemical impedance spectroscopy (EIS) was performed as shown in Figure 3b. The equivalent circuit model was used to elucidate the Nyquist plot of Ti-Fe_2O_3, Ti-(SiO_x/Fe_2O_3), and Ti-(SiO_x/np-Fe_2O_3) (further details for several anodes are given in the Supporting Information, Figure S16). The resistance of the electrolyte–semiconductor interface (R_2) of the Ti-(SiO_x/Fe_2O_3) and Ti-(SiO_x/np-Fe_2O_3) was lower than that of Ti-Fe_2O_3, indicating superior charge-transfer properties from the Ti-Fe_2O_3 to the electrolyte with low recombination due to the good OER properties of the Ti-SiO_x layer for the water oxidation. The reduced recombination was confirmed by calculating the carrier life time from the decay of the transient open circuit potential (Supporting Information, Figure S17). The electron carrier lifetime of the Ti-SiO_x layer containing samples much higher than those of the other samples indicates that the Ti-SiO_x layer can passivate the surface states of the Ti-Fe_2O_3 and decrease the recombination. The effect of the presence of the nanoporous structure of hematite for PEC was also confirmed by comparing the EIS data of Ti-(SiO_x/np-Fe_2O_3) and Ti-(SiO_x/Fe_2O_3). The R_2 value of Ti-(SiO_x/Fe_2O_3) was higher than that of Ti-(SiO_x/np-Fe_2O_3), which indicates that nanoporous structures enhance the charge transfer between the electrolyte and the hematite (blue vs. red) by shortening the

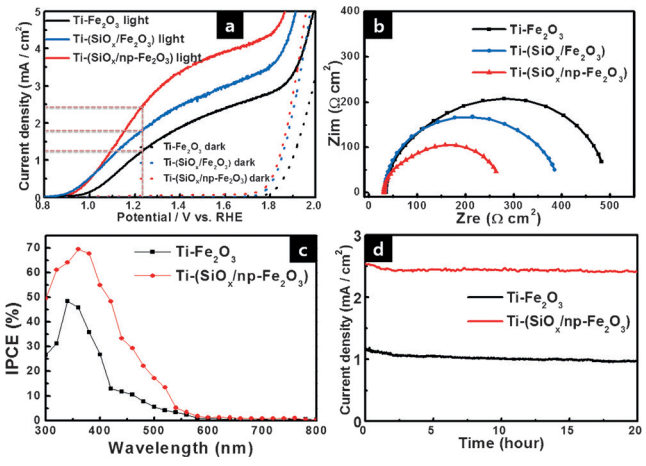

Figure 3. Photoelectrochemical performance of as-prepared samples in a 1 M NaOH solution at 1.23 V_{RHE}. a) *J*–*V* curves of Ti-Fe_2O_3, Ti-(SiO_x/Fe_2O_3), and Ti-(SiO_x/np-Fe_2O_3) under one-sun illumination and dark conditions with a three-electrode system. b) EIS analysis of Ti-Fe_2O_3, Ti-(SiO_x/Fe_2O_3), and Ti-(SiO_x/np-Fe_2O_3) at 1.23 V_{RHE}. c) IPCE data of the Ti-Fe_2O_3 and Ti-(SiO_x/np-Fe_2O_3) at 1.23 V_{RHE}. d) The stability data of Ti-Fe_2O_3 and Ti-(SiO_x/np-Fe_2O_3) for 20 h at 1.23 V_{RHE}.

hole-diffusion pathway.[6b] The R_s of the Ti-(SiO_x/np-Fe_2O_3) was similar to (slightly lower than, in fact) that of the others which indicated that the Ti-SiO_x layer did not greatly affect the bulk resistance in the Ti-Fe_2O_3. The IPCE data in Figure 3c shows a higher photocurrent density of Ti-(SiO_x/np-Fe_2O_3) compared to that of Ti-Fe_2O_3 in a range from 300 nm to 550 nm at 1.23 V_{RHE} with a 1M NaOH solution due to the synergetic effect of short hole-diffusion pathways, a high surface area, and decreased recombination by the passivation layer. Figure 3d displays the stability of the Ti-(SiO_x/np-Fe_2O_3) and Ti-Fe_2O_3 at 1.5 V_{RHE} under AM 1.5 with the 1M NaOH solution (pH 13.6) for 20 h. After 20 h, the photocurrent density of Ti-(SiO_x/np-Fe_2O_3) was still 2.41 mA cm^{-2}, which confirmed the chemical inertness of the Ti-SiO_x layer. Furthermore, the chemical composition of the Ti-SiO_x did not change after the 20 h stability test, except the increase in OH^- ion concentration that helped enhance the OER properties of Ti-SiO_x coated hematite, as explained in the previous section (Supporting Information, Figure S12).

To further increase the PEC performance of the Ti-(SiO_x/np-Fe_2O_3) photoanode, a well-known water oxidation catalyst for Fe_2O_3, cobalt phosphate (Co-Pi) nanoparticles were deposited on hematite by a modified photoassisted electrodeposition method.[22] The 2–5 nm of the Co-Pi nanoparticles were well attached on the surface of the Ti-Fe_2O_3 and Ti-(SiO_x/np-Fe_2O_3) as shown in Figures 4a,b. When Co-Pi was applied to Ti-(SiO_x/np-Fe_2O_3), the photocurrent density of Co-Pi/Ti-(SiO_x/np-Fe_2O_3) reached 3.19 mA cm^{-2} at 1.23 V_{RHE} and 3.70 mA cm^{-2} at 1.50 V_{RHE}, as shown in Figure 4c (dotted line), which is comparable to that of 3D-hematite nanowires having the reliable record current (3.39 mA cm^{-2} at 1.23 V_{RHE}).[23] Furthermore, the onset potential was cathodically shifted for Co-Pi/Ti-(SiO_x/np-Fe_2O_3) from 0.95 V_{RHE} to 0.80 V_{RHE}. It should be noted that Ti-(SiO_x/np-Fe_2O_3) was prepared by a simple dip-coating and sintering process and did not require complex fabrication methods such as patterning, etching, spray coating, and sintering, which are needed to fabricate 3D-hematite nanowires.[23,24] Note that although the Co-Pi nanoparticles were deposited on the surface of Ti-Fe_2O_3, the surface states on the surface of hematite existed consistently as shown in the upper image of Figure 4d. The PEC performance of the Co-Pi/Ti-Fe_2O_3 was still deteriorated by the charge recombination due to the remaining surface states of hematite. However, as shown in the bottom model of Figure 4d, when surface states of hematite in Co-Pi/Ti-Fe_2O_3 were reduced by the Ti-SiO_x passivation layer (Co-Pi/Ti-(SiO_x/np-Fe_2O_3)), the effect of the Co-Pi in PEC cells dramatically increased (dotted line vs. dashed line). These results demonstrate that Co-Pi/Ti-(SiO_x/np-Fe_2O_3) could take full advantage of the synergetic effect of the surface passivation layer, direct hole extraction, high surface area, short hole-diffusion pathway from hematite to electrolyte, and superior OER co-catalyst for high performance of water splitting systems.

In conclusion, we report a high PEC performance hematite photoanode coated with the Ti-SiO_x passivation layer fabricated by a simple dip coating/high temperature annealing process. This process not only created the 2–5 nm thin Ti-SiO_x passivation layer on Ti-Fe_2O_3 but also generated the nanopores inside the Ti-Fe_2O_3, which increased the number of reaction sites for water oxidation. The Ti-(SiO_x/np-Fe_2O_3) photoanode has a photocurrent density of 2.44 mA cm^{-2} at 1.23 V_{RHE} and 3.70 mA cm^{-2} at 1.50 V_{RHE}. We attributed this enhanced photocurrent density to the superior charge extraction properties and proper conductivity of the Ti-SiO_x layer, the reduced recombination from the protected surface states of Ti-Fe_2O_3, and the porous morphology providing a short hole-diffusion pathway. The stability of Ti-(SiO_x/np-Fe_2O_3) was also enhanced by the high chemical inertness of the Ti-SiO_x layers. When a Co-Pi co-catalyst was applied to Ti-(SiO_x/np-Fe_2O_3), the photocurrent density reached 3.19 mA cm^{-2} at 1.23 V_{RHE} with a cathodic shift of onset potential from 0.95 to 0.80 V_{RHE}. Our study presents a straightforward approach for achieving highly efficient and stable PEC systems without a complex and expensive fabrication method.

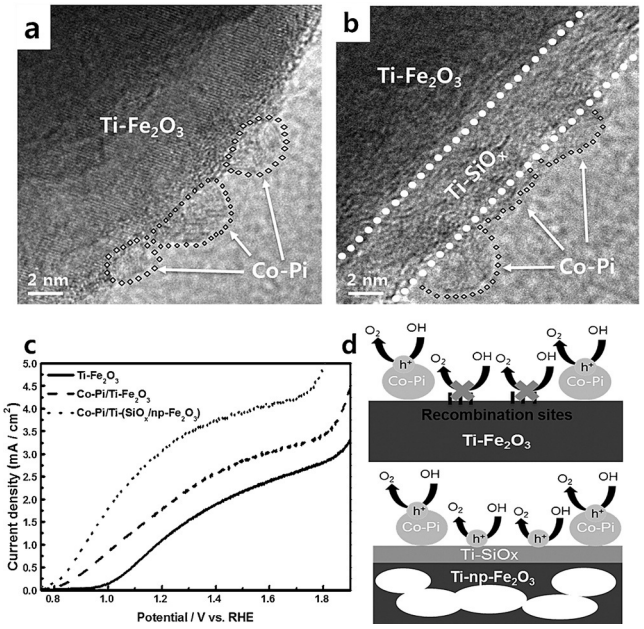

Figure 4. a) TEM image of the Co-Pi/Ti-Fe_2O_3, and b) Co-Pi/Ti-(SiO_x/np-Fe_2O_3). c) *J–V* curves of the reference Ti-Fe_2O_3, Co-Pi/Ti-Fe_2O_3, and Co-Pi/Ti-(SiO_x/np-Fe_2O_3) under one-sun conditions in 1M NaOH solution with a three-electrode system. d) The reaction mechanism of Co-Pi/Ti-Fe_2O_3 (upper image) and Co-Pi/Ti-(SiO_x/np-Fe_2O_3) (bottom image).

Acknowledgements

This work is supported by NRF with the contract no. NRF-2015-R1A2A2A01005250, by IBS-R019-D1, and by the Materials and Components Technology Development Program of MOTIE/KEIT (Republic of Korea) with the contract number of 10062092.

Keywords: conductive SiO_x layers · hematite · nanoporous structures · passivation layers · photoelectrochemical cells

How to cite: *Angew. Chem. Int. Ed.* **2016**, *55*, 9922 – 9926
Angew. Chem. **2016**, *128*, 10076 – 10080

[1] S. Chu, A. Majumdar, *Nature* **2012**, *488*, 294 – 303.
[2] a) J. Y. Kim, G. Magesh, D. H. Youn, J.-W. Jang, J. Kubota, K. Domen, J. S. Lee, *Sci. Rep.* **2013**, *3*, 2681; b) A. Fujishima, K. Honda, *Nature* **1972**, *238*, 37 – 38.
[3] a) N. Liu, C. Schneider, D. Freitag, M. Hartmann, U. Venkatesan, J. Müller, E. Spiecker, P. Schmuki, *Nano Lett.* **2014**, *14*, 3309 – 3313; b) H. Chen, Z. Wei, K. Yan, Y. Bai, Z. Zhu, T. Zhang, S. Yang, *Small* **2014**, *10*, 4760 – 4769; c) K.-Y. Yoon, H.-J. Ahn, M.-J. Kwak, P. Thiyagarajan, J.-H. Jang, *Adv. Opt. Mater.* **2015**, *3*, 907 – 912; d) K. Sivula, F. Le Formal, M. Grätzel, *ChemSusChem* **2011**, *4*, 432 – 449; e) Y. Li, T. Takata, D. Cha, K. Takanabe, T. Minegishi, J. Kubota, K. Domen, *Adv. Mater.* **2013**, *25*, 152 – 152; f) H.-J. Ahn, M.-J. Kim, K. Kim, M.-J. Kwak, J.-H. Jang, *Small* **2014**, *10*, 2325 – 2330.
[4] O. Zandi, B. M. Klahr, T. W. Hamann, *Energy Environ. Sci.* **2013**, *6*, 634 – 642.
[5] a) F. J. Morin, *Phys. Rev.* **1951**, *83*, 1005 – 1010; b) J. A. Glasscock, P. R. F. Barnes, I. C. Plumb, N. Savvides, *J. Phys. Chem. C* **2007**, *111*, 16477 – 16488; c) M. Barroso, S. R. Pendlebury, A. J. Cowan, J. R. Durrant, *Chem. Sci.* **2013**, *4*, 2724 – 2734.
[6] a) K.-Y. Yoon, J.-S. Lee, K. Kim, C. H. Bak, S.-I. Kim, J.-B. Kim, J.-H. Jang, *ACS Appl. Mater. Interfaces* **2014**, *6*, 22634 – 22639; b) H.-J. Ahn, M.-J. Kwak, J.-S. Lee, K.-Y. Yoon, J.-H. Jang, *J. Mater. Chem. A* **2014**, *2*, 19999 – 20003.
[7] L. Xi, S. Y. Chiam, W. F. Mak, P. D. Tran, J. Barber, S. C. J. Loo, L. H. Wong, *Chem. Sci.* **2013**, *4*, 164 – 169.
[8] T. Hisatomi, F. Le Formal, M. Cornuz, J. Brillet, N. Tetreault, K. Sivula, M. Grätzel, *Energy Environ. Sci.* **2011**, *4*, 2512 – 2515.
[9] F. Le Formal, N. Tetreault, M. Cornuz, T. Moehl, M. Gratzel, K. Sivula, *Chem. Sci.* **2011**, *2*, 737 – 743.
[10] a) Y. Hou, F. Zuo, A. Dagg, P. Feng, *Nano Lett.* **2012**, *12*, 6464 – 6473; b) H.-J. Ahn, K.-Y. Yoon, M.-J. Kwak, J.-S. Lee, P. Thiyagarajan, J.-H. Jang, *J. Mater. Chem. A* **2015**, *3*, 21444 – 21450; c) Y.-C. Wang, C.-Y. Chang, T.-F. Yeh, Y.-L. Lee, H. Teng, *J. Mater. Chem. A* **2014**, *2*, 20570 – 20577.
[11] a) R. H. Goncalves, E. R. Leite, *Energy Environ. Sci.* **2014**, *7*, 2250 – 2254; b) T. P. Almeida, M. W. Fay, T. W. Hansen, Y. Zhu, P. D. Brown, *CrystEngComm* **2014**, *16*, 1540 – 1546; c) I. C. Masthoff, A. Gutsche, H. Nirschl, G. Garnweitner, *CrystEngComm* **2015**, *17*, 2464 – 2470.
[12] a) A. Kim, S. Lim, D.-H. Peck, S.-K. Kim, B. Lee, D. Jung, *Nanomaterials* **2012**, *2*, 206; b) P. Zhu, M. Teranishi, J. Xiang, Y. Masuda, W.-S. Seo, K. Koumoto, *Thin Solid Films* **2005**, *473*, 351 – 356.
[13] Y. Ling, G. Wang, J. Reddy, C. Wang, J. Z. Zhang, Y. Li, *Angew. Chem. Int. Ed.* **2012**, *51*, 4074 – 4079; *Angew. Chem.* **2012**, *124*, 4150 – 4155.
[14] X. Gou, G. Wang, X. Kong, D. Wexler, J. Horvat, J. Yang, J. Park, *Chem. Eur. J.* **2008**, *14*, 5996 – 6002.
[15] P. Zhang, L. Gao, X. Song, J. Sun, *Adv. Mater.* **2015**, *27*, 562 – 568.
[16] J. R. Shallenberger, *J. Vac. Sci. Technol. A* **1996**, *14*, 693 – 698.
[17] a) D. Noguchi, T. Sakai, T. Nagatomo, *J. Ceram. Soc. Jpn.* **2005**, *113*, 630 – 633; b) L. Bousse, S. Mostarshed, B. Van Der Shoot, N. F. de Rooij, P. Gimmel, W. Göpel, *J. Colloid Interface Sci.* **1991**, *147*, 22 – 32.
[18] J. Y. Kim, J.-W. Jang, D. H. Youn, G. Magesh, J. S. Lee, *Adv. Energy Mater.* **2014**, *4*, 1400476.
[19] P. Zhang, A. Kleiman-Shwarsctein, Y.-S. Hu, J. Lefton, S. Sharma, A. J. Forman, E. McFarland, *Energy Environ. Sci.* **2011**, *4*, 1020 – 1028.
[20] a) C. Schindler, S. C. P. Thermadam, R. Waser, M. N. Kozicki, *IEEE Trans. Electron Devices* **2007**, *54*, 2762 – 2768; b) H. Na, J. Oh, K. Lee, J. Kim, S. Lee, D. H. Lim, M.-H. Cho, H. Sohn, *Microelectron. Eng.* **2013**, *110*, 6 – 11.
[21] J. Brillet, M. Grätzel, K. Sivula, *Nano Lett.* **2010**, *10*, 4155 – 4160.
[22] D. K. Zhong, M. Cornuz, K. Sivula, M. Gratzel, D. R. Gamelin, *Energy Environ. Sci.* **2011**, *4*, 1759 – 1764.
[23] J. Li, Y. Qiu, Z. Wei, Q. Lin, Q. Zhang, K. Yan, H. Chen, S. Xiao, Z. Fan, S. Yang, *Energy Environ. Sci.* **2014**, *7*, 3651 – 3658.
[24] Y. Qiu, S.-F. Leung, Q. Zhang, B. Hua, Q. Lin, Z. Wei, K.-H. Tsui, Y. Zhang, S. Yang, Z. Fan, *Nano Lett.* **2014**, *14*, 2123 – 2129.

Received: April 22, 2016
Revised: May 20, 2016
Published online: June 30, 2016

